Applied Clay Science 227 (2022) 106591

Contents lists available at ScienceDirect

Applied Clay Science

journal homepage: www.elsevier.com/locate/clay

Research paper

Detection of Cr(III), prometryn, and ibuprofen by hybrid Eu(III)–dipicolinate kaolinite luminescent sensor

F.C. Clementino [a], V.G. Peixoto [a], D.T. de Araújo [a], K.J. Ciuffi [a], E.J. Nassar [a], M.A. Vicente [b,*], V. Rives [b], E.H. de Faria [a,*]

[a] Grupo de Pesquisas em Materiais Lamelares Híbridos (GPMatLam), Universidade de Franca, 14404–600 Franca, São Paulo, Brazil
[b] GIR–QUESCAT, Departamento de Química Inorgánica, Universidad de Salamanca, 37008 Salamanca, Spain

ARTICLE INFO

Keywords:
Kaolinite
Lanthanide complexes
Eu(III) luminescence
Metallic pollutants
Organic pollutants
Pollutants detection

ABSTRACT

Europium (III) was complexed on solids prepared by kaolinite functionalization with pyridine 2–carboxylic and pyridine 2,6–dicarboxylic acids; the luminescent properties of the obtained solids were analyzed for evaluating their application as luminescent sensors of prometryn, ibuprofen and chromium (III). The luminescent hybrid materials were characterized through powder X–ray diffraction, infrared absorption spectroscopy, thermal analysis, scanning electron microscopy, ultraviolet/visible absorption spectroscopy, energy dispersion and photoluminescence spectroscopy (excitation and emission) and lifetime measurements of the excited state. The materials proved to be promising, with quantum efficiencies of 31.16% and 45.18% for the samples functionalized with picolinic and dipicolinic acids, respectively. For the contaminant adsorption tests, the solid with picolinic acid showed better detection efficiency in a lower concentration range for chromium (III) than solids with dipicolinic acid, while both showed similar ranges for the organic contaminants.

1. Introduction

Technologies that allow the identification and monitorization of contaminants in water are of general interest for ensuring the quality control of surface and underground drinking water (Sharma and Bhattacharya, 2017). Among the various "conventional" pollutants found in water, heavy metal ions show a high toxicity, they are not biodegradable; having a cumulative effect on the human body (Liu et al., 2017). In addition to the conventional contaminants, the new class known as "emerging pollutants", as drugs and pesticides, has recently attracted the attention of researchers. These contaminants are usually present in low concentrations and cannot be removed by traditional treatments, causing new problems to human health and to the environment (Peña-Guzmán et al., 2019; Tang et al., 2020).

In this context, new sensors for detecting chromium (III), ibuprofen and prometryn are studied in this work. The toxicokinetic of chromium compounds depends on the oxidation state of the metal [(III) or (VI)]. Hexavalent chromium easily penetrates cells, while trivalent chromium can be absorbed by phagocytosis (Shanker et al., 2005; Danish et al., 2019). The toxic effects promoted by Cr(VI) include its carcinogenic action on human beings, attributed to dermatoses, kidney injuries, etc. (Yang et al., 2019). Ibuprofen is a drug widely used as an anti–inflammatory, antipyretic and analgesic agent that has been frequently detected in different environmental matrices, making it one of the most common emerging contaminant drugs in aquatic environments (Di Baccio et al., 2017). Finally, the accumulation in aquatic environments of prometryn, a triazine herbicide among the most widely used worldwide, represents a real risk to wildlife, the environment and human health (Gonzalez-Rey et al., 2015).

Detection of these contaminants in low concentrations is a priority issue for environmental protection. The strategies for the control and detection of these pollutants have as a prerequisite the construction of highly sensitive and selective devices (Jia et al., 2020), that can be based on different technologies; for instance, electronics (Mbokana et al., 2020), electrochemistry (Dorledo de Faria et al., 2020) or optics (Wang et al., 2016). In particular, optical sensors have several attractive features such as the easiness of integration into microfluidic platforms (Bates and Lu, 2016) and the ability to monitor extremely complex hazardous environments. Among them, fluorescent sensors have gained popularity in recent years for providing high specificity, as well as low detection limits, fast response time and technical simplicity. In this case, the sensors based on lanthanide ions are promising due to their peculiar

* Corresponding authors.
E-mail addresses: mavicente@usal.es (M.A. Vicente), emerson.faria@unifran.edu.br (E.H. de Faria).

https://doi.org/10.1016/j.clay.2022.106591
Received 17 January 2022; Received in revised form 5 April 2022; Accepted 30 May 2022
Available online 6 June 2022

spectroscopic characteristics, which are mainly due to the electronic transitions within the 4f shell (Su et al., 2019). Their bands in the electronic spectra are narrow and generally do not show significant energy shifts as the 4f orbitals are "shielded" from interactions with the ligands through the outermost 5 s and 5p filled orbitals (Binnemans, 2009). However, even with promising properties, the use of lanthanide complexes is still limited, mainly due to their low thermal, photochemical and mechanical stability (Utochnikova, 2019).

For sorting out these problems, the use of these complexes in organo–functionalized inorganic matrices has been investigated (De Araujo et al., 2017; Xiang et al., 2017). These hybrid materials can be classified according to the sort of interaction established between the organic and inorganic phases: *Class I* Hybrid, where the interaction between the components formed is by hydrogen bonds, Van der Waals forces or simple electrostatic interactions; and *Class II* hybrids, having strong chemical interactions between their components (covalent bond) (Jasrotia et al., 2019). The intensity of this interaction force is also one of the decisive factors for their thermal, magnetic, optical, mechanical, or chemical properties, among others.

The strategy synthesis adopted for development of hybrid materials could influence drastically the properties and thus the final application of this type of solids, e.g., hybrid class I obtained via hydrogen bonds or weaker van der Waals forces may suffer leaching of active species, directly conditioning sensing application. This fact corroborates the displacing method of kaolinite and subsequently functionalization with pyridine–carboxylic acids using the melting of organic ligands to be the best choice (De Faria et al., 2009). The melting of organic ligands pyridine carboxylic acids and kaolinite results in type Al–O–C covalent bonds that contribute to chemical stability in applications involving aqueous medium.

Inorganic–organic hybrid luminescent materials based on natural clay minerals are extremely attractive for these purposes due to: (i) the very sharp and intense 4f transitions of lanthanide complexes, they can be tuned to detect only specific analytes, and (ii) their specific properties, such as chemical affinity for smectite clay minerals for cations (Whittaker et al., 2019) and layered double hydroxides for anions (Rives, 2001), thus offering good selectivity to electrically–charged contaminants. The use of specific organic groups to graft the interlayer space of layered solids increases these characteristics promoting the chemical selectivity required by sensing systems, pyridine carboxylic acids have found to be excellent groups for these purposes, completing the lanthanide coordination sphere and providing structural rigidity (de Faria et al., 2011; Chen et al., 2017; De Araujo et al., 2017; Xiang et al., 2017; Wang et al., 2019). The resulting materials showed higher thermal stability and quantum efficiency than the isolated complexes, and their synthesis was viable and reproducible.

The luminescent performance of lanthanide complexes/clay minerals hybrid materials is receiving increasing attention, although practical applications have been scarcely explored. For example, Lezhnina et al. (2007) have described the intercalation of 2,2′–bypyridine–Tb^{3+} complexes in the hectorite interlayer space; Li et al. (2016) reported the ratiometric detection of low–level water in organic solvents based on Eu^{3+}– and Tb $^{3+}$–acetylacetonate complexes intercalated in Laponite®, Tronto et al. (2009) reported the cation exchange of lanthanides in Laponite®; Sas et al. (2015) reported the immobilization of the organic fluorescent dye rhodamine B in kaolinite using the grafting strategy; Ma et al. (2019) reported very interesting self–healing and luminescent materials using synthetic Laponite® nanoclay (Ma et al., 2019); while Marchesi et al. (2021) have reported the enhancement of the luminescence properties of Eu (III) in paramagnetic saponites. On the other hand, sensors based on clays have been used, mainly on electroanalytical methods. For example, Sato et al. (2014) reported an oxygen sensor based on Ir(II)) complexes and clay minerals (saponite, montmorillonite and hectorite) and Aydar et al. (2018) reported a hydroquinone sensor based on nano–sepiolite. However, the use of lanthanide–based sensors is much more scarce, and only Chen et al. (2017) have reported the use of an Eu(III)–dipicolinic acid–Laponite inorganic hybrid material for discrimination of glutathione.

Up to our best knowledge, luminescence sensors based on lanthanide cations immobilized on clay minerals have not been used for detection of aqueous pollutants. In this context, Eu(III) cations have been incorporated into kaolinite–picolinic acids hybrid materials to investigate their luminescence in contact with inorganic and organic pollutants in order to obtain chemical sensors capable of effectively detecting these contaminants.

2. Experimental section

2.1. Materials

Kaolinite from São Simão, state of São Paulo (Brazil), kindly supplied by the mining company Darcy R.O. Silva e Cia and purified by dispersion–decantation was used as parent material, being named as Kaol. The chemical formula of kaolinite calculated from ICP/OES was $Si_{2.0}Al_{1.96}Fe_{0.03}Mg_{0.01}K_{0.02}Ti_{0.03}O_{7.06}$ (De Faria et al., 2009). The kaolinite derivative intercalated with dimethylsulfoxide (DMSO), Kaol–DMSO, was obtained by dispersing purified kaolinite in DMSO and H_2O (Dedzo and Detellier, 2016).

The materials functionalized with pyridine 2–carboxylic (picolinic) acid (Pa) and pyridine 2,6–dicarboxylic (dipicolinic) acid (Dpa) were obtained by melting a mass of the carboxylic acid in the presence of the Kaol–DMSO precursor, in a mass ratio of 5:1 (de Faria et al., 2011, 2012; de Araujo et al., 2017), the solids obtained were denoted as Kaol–Pa and Kaol–Dpa, respectively.

2.2. Europium (III) adsorption tests

A $5.00{\cdot}10^{-2}$ mol L^{-1} $EuCl_3{\cdot}6H_2O$ in water parent solution was prepared, diluted to concentrations between $1.00{\cdot}10^{-3}$ to $3.00{\cdot}10^{-2}$ mol L^{-1}, and then mixed (1:1 *v*/v) with xylenol orange ($5{\cdot}10^{-5}$ mol L^{-1}) (Takahashi, 1964). The calibration curve was constructed from their UV–Vis absorption spectra, fixing the absorbance at 394 nm, transition $^7F_0 \rightarrow {}^5L_6$ of the europium (III) ion ($R = 0.98926$).

2.2.1. Kinetic study

An amount of 2 mL of $EuCl_3{\cdot}6H_2O$ ($5{\cdot}10^{-2}$ mol L^{-1}) was placed in contact with $1{\cdot}10^{-2}$ g of the Kaol–Pa and Kaol–Dpa matrices, kept under constant agitation and collected after 1, 3, 5, 7, 10, 15, 30, 60, 120, 240, 480, 1440, 2880, 4320 and 5760 min. The pH of the solution was not externally modified, and it was close to 4.5. After filtration, the resulting solutions were mixed with the xylenol orange solution under the same conditions as for the calibration curve and their UV–Vis absorption spectra were recorded.

2.2.2. Equilibrium study

The tests were carried out by dispersing $1{\cdot}10^{-2}$ g of the Kaol–Pa or Kaol–Dpa matrices in 2 mL of adsorbate solution, with concentrations of $1{\cdot}10^{-3}$; $2{\cdot}10^{-3}$; $4{\cdot}10^{-3}$; $8{\cdot}10^{-3}$; $1{\cdot}10^{-2}$; $2{\cdot}10^{-2}$; $4{\cdot}10^{-2}$; $5{\cdot}10^{-2}$ and $8{\cdot}10^{-2}$ mol L^{-1}. The dispersion was kept in constant agitation and for each adsorption experiment the supernatant liquid was separated from the powder at the interval times previously established in the kinetic study (see above) for each sample (Kaol–Pa and Kaol–Dpa). The pH was ~4.5. The resulting solution was analyzed by UV–Vis spectroscopy and the adsorption capacity of the samples was calculated based on calibration curves of each contaminant.

2.3. Synthesis of the luminescent materials

A solution of $EuCl_3{\cdot}6H_2O$ was added to 0.38 g of the precursor compound, under the same conditions used in the kinetic study, the times of adsorption being 24 h for Kaol–Pa and 48 h for Kaol–Dpa. The concentrations of $EuCl_3{\cdot}6H_2O$ solutions were established from the Eu

(III) adsorption equilibrium study, and corresponded to $5{\cdot}10^{-2}$ mol L^{-1} for Kaol–Pa and $8{\cdot}10^{-2}$ mol L^{-1} for Kaol–Dpa. The materials obtained were centrifuged and dried in an oven at 60 °C. The resulting materials were designated as Eu(Kaol–Pa) and Eu(Kaol–Dpa).

2.4. Application of luminescent materials as chemical sensors

As indicated, the synthesized luminescent hybrid materials, Eu (Kaol–Pa) and Eu(Kaol–Dpa), were tested against three potentially polluting products: Cr^{3+} (from $CrCl_3{\cdot}6H_2O$), the drug ibuprofen and the herbicide prometryn. Calibration curves of the pollutant stock solutions were determined and $7{\cdot}10^{-2}$ g of each of the synthesized materials was used to perform the tests. A 5 mL aliquot of the solutions containing 1 g L^{-1} of $CrCl_3{\cdot}6H_2O$, ibuprofen (0.1 g L^{-1}) and prometryn (0.01 g L^{-1}) was pipetted and left in contact with the materials for 1 min. Then, the dispersion was centrifuged, the resulting solution was separated and the solid was dried. The pH during the adsorption experiments was close to 4.5. The luminescent behavior of the solid after drying was analyzed, in order to establish a correlation with the amount of pollutant adsorbed. This procedure was repeated for periods of contact time of 7, 15, 30, 60 and 120 min.

2.5. Characterization techniques

The powder X–ray diffractograms were obtained at the Analytical Center of the University of Franca on a Miniflex II–RIGAKU equipment, at 40 kV and 30 mA (1200 W). A copper tube was used (radiation CuKα = 1.54051 Å), scanning 2θ angles ranging from 2 to 75° at a scan speed of 10°/min, over microcrystalline powder samples.

The infrared absorption spectra were recorded on a Perkin–Elmer 1730 Frontier spectrophotometer with FT Fourier Transform, the analyzed spectral range was 4000 to 400 cm^{-1}, with a nominal resolution of 1 cm^{-1}, and accumulating 32 scans. The samples were analyzed by the diffuse reflectance technique by mixing with KBr, using KBr itself as a background. After the photoluminescence sensing tests, new spectra were recorded mixing 995 mg of KBr and 5.0 mg of the solids containing the adsorbed contaminants, prometryn, ibuprofen and Cr^{3+} (quantitative spectra).

Thermal analyses were carried out using a TA Instruments SDT Q600 Simultaneous DTA–TGA thermal analysis apparatus, in the temperature range of 25 °C and 800 °C, in a dynamic synthetic air atmosphere with a flow rate of 100 mL/min and heating rate of 20 °C per minute.

The Scanning Electron Microscopy images were obtained in a Tescan Vega 3 Model EasyProbe. The samples were dispersed in the stub with carbon tape and afterwards were coated with a thin layer of gold by a Quorum SC7620 coating system. The average diameter size of the particles was calculated using the ImageJ software (https://imagej.nih.gov/ij).

The absorption spectra in the ultraviolet/visible region were obtained in a Diode Array UV–Vis HP 8453 Spectrophotometer, using a quartz cuvette with 10 mm optical path.

The excitation and emission spectra were recorded in 450 W xenon continuous light, in a 25 W Xenon pulsed lamp to determine the lifetime values, using a Horiba Jobin Yvon Fluorolog spectrofluorimeter. All analyses were performed with a 45° detection angle at room temperature. For the excitation spectra, Corning 97,202 filters were used with transmittance less than 0.2% below 470 nm; the excitation and emission slits are described in the legend of each spectrum.

3. Results and discussion

3.1. Characterization of hybrid materials

Purified kaolinite had the basal reflection at 7.12 Å, which after treatment with DMSO increased to 10.58 Å (Fig. 1), with an expansion of 3.46 Å, a value compatible with the diameter of the inserted molecule (Brandt et al., 2003; Lapides and Yariv, 2009; Dedzo and Detellier, 2016; Ferreira et al., 2017).

The precursor material Kaol–DMSO had the highest intercalation rate, 70% (Table 1), due to the fact that DMSO molecule is highly polar and has a small diameter, which facilitated its incorporation into the clay mineral and the formation of stable interactions as hydrogen bonds into the interlayer space (Mbey et al., 2013). On the other hand, hybrid materials presented lower values for this rate, since picolinic acids needed to occupy the expanded Kaol–DMSO interlayer spaces after displacement of the DMSO molecules. The crystallinity ratio of the materials decreased with the treatments, pure kaolinite showing the highest R value, 1.43, i. e., all the treated materials were less crystalline than parent kaolinite (Table 1) (Brandt et al., 2003).

Crystallinity values, including the FWHM index, strongly supported that picolinic and dipicolinic acids promoted the delamination of the kaolinite structure or, at least, did not favor the stacking; probably, the

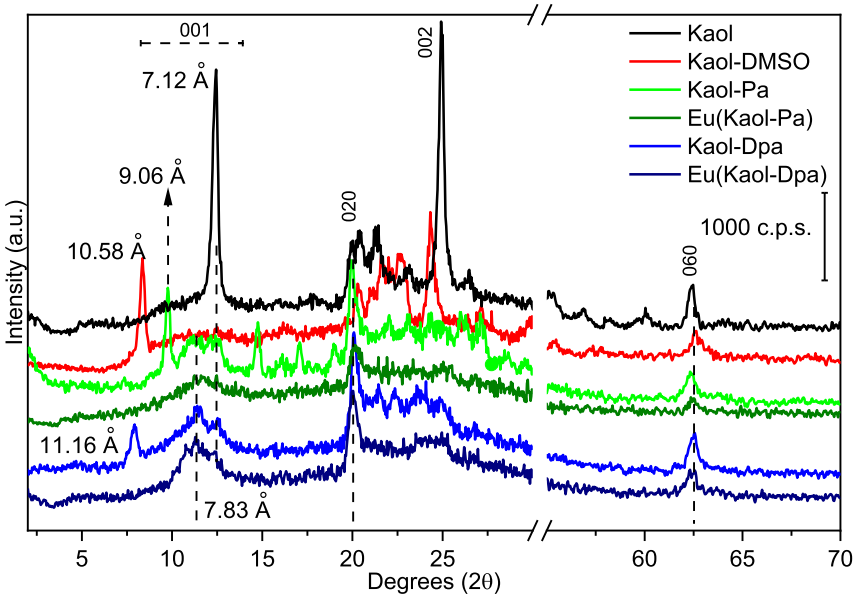

Fig. 1. X–ray diffractograms of the hybrid materials.

Table 1
Basal d_{001} value, basal value variation (Δd_{001}), intercalation/functionalization rate (α), crystallinity ratio (R) and full–width half maximum d_{001} (FWHM) of the different samples.

Sample	d_{001}(Å)	Δd_{001}(Å)	α[a] (%)	R[b]	FWHM (2θ)
Kaol	7.12	–	–	1.43	0.34
Kaol–DMSO	10.58	3.46	70	1.26	0.35
Kaol–Pa	9.06/7.83	1.95/0.71	61/50	0.85	0.36/2.76
Kaol–Dpa	11.16/7.83	4.05/0.71	48/54	0.44	0.40/2.76
Eu(Kaol–Pa)	7.83	0.71	50	0.68	2.72
Eu(Kaol–Dpa)	7.83	0.71	54	0.65	2.48

[a] Calculated as $\alpha = I/[I + I_o]$, I being the intensity of the reflection in an intercalated sample and I_o the intensity of the same reflection in the non–reacted kaolinite.
[b] Calculated as $R = I_{001}/I_{020}$, I_{001} and I_{020} being the intensities of the corresponding reflections.

presence of these compounds on the surface of the layers prevented formation of hydrogen bonds and decreased the strength cohesion between the layers.

As the incorporation of the acids was done by displacement of DMSO, such a displacement may not be complete. The 060 reflection at 62.5° (2θ), representative of the dioctahedral clay mineral, showed that the individual structure of the layers was not affected by the reaction processes (Letaief and Detellier, 2007; Tonlé et al., 2007; Letaief et al., 2008). After the complexation process, the basal value for the Pa–containing solids was altered, suggesting a breakdown of the tactoids in the complexed regions, so that the complex occupied the matrix surface while the molecules that were not covalently bonded to kaolinite surface could be leached.

The OH stretching region in the infrared spectrum of kaolinite is very sensitive to the effects of interlayer modification (Tunney and Detellier, 1996). Consequently, both intercalation with DMSO and functionalization with pyridine carboxylic acids modified the stretching pattern of the kaolinite OH groups (Fig. 2). The bands at 3695 (OH4 in Fig. 2), 3669 (OH2), and 3653 (OH3) cm^{-1} in the spectrum of Kaol corresponded to interlamellar hydroxyls, and the band at 3620 cm^{-1} corresponded to intralamellar hydroxyls (Tunney and Detellier, 1996; De Araujo et al., 2017). The bands due to the stretching modes of hydrogen bonds between the silicon ions outside and in the plane were recorded at 700 and 472 cm^{-1}, respectively; the bands due to Si—O stretching modes were recorded between 1000 and 1200 cm^{-1}, while the band at 423 cm^{-1} was attributed to angular vibration. The bands due to stretching vibrations of interlamellar and intralamellar aluminol groups were recorded at 938 and 914 cm^{-1} (Frost, 1996; De Faria et al., 2009; Da Silva et al., 2016).

After intercalation of the purified kaolinite with DMSO, the interlayer hydroxyls of kaolinite interacted with the intercalating molecules through formation of hydrogen bonds with their sulfoxide groups, which resulted in the shift of the bands due to these hydroxyls to 3541 and 3504 cm^{-1} (Zhang et al., 2014). In the region where the bands due to the vibrations of inter and intralamellar hydroxyls are expected, the bands at 3669 and 3653 cm^{-1} were absent in the spectra of the hybrid materials, which suggested the binding of the pyridine carboxylic acid group to kaolinite, forming a sort of surface picolinate. The spectra also showed the characteristic bands of anti–symmetric and symmetric stretching modes of the carboxylate group at 1698, 1571 and 1449 cm^{-1}, emphasizing the kaolinite functionalization.

After complexation with the Eu^{3+}, no change was observed in the characteristic vibrations of the intralamellar (3622 cm^{-1}) and interlamellar (3698 cm^{-1}) OH groups, showing that the molecules of the pyridine–carboxylic acids remained functionalized. The characteristic bands of picolinic acids, such as those due to the pyridine–carboxylic ring, symmetric and anti–symmetric stretching of the carboxylate group (1449, 1571, 1698 and 1354 cm^{-1} for sample Kaol–Pa and 1454, 1570, 1650, 1380 cm^{-1} for sample Kaol–Dpa) were shifted to higher wavenumbers, being recorded at 1478, 1570, 1653 and 1350 cm^{-1} for sample Eu(Kaol–Pa) and at 1488, 1570, 1653, 1340 cm^{-1} for Eu(Kaol–Dpa). This fact confirmed the successful complexation of the Eu^{3+} species in the matrices, by interaction between the complexed Eu^{3+} ion and the carboxylates (De Faria et al., 2011; De Araujo et al., 2017).

Purified kaolinite showed in the thermogravimetric analysis (Fig. 3) a first mass loss step (14%), with a maximum mass loss at 523 °C, due to kaolinite dehydroxylation and formation of metakaolin (Brandt et al., 2003; Avila et al., 2010). For the Kaol–DMSO sample, four stages of mass loss were found: at 68 °C (8%) and 106 °C (11.5%), both attributed to the removal of ethanol and water present on the surface and in the interlayer space; 183 °C (15%), corresponding to the elimination of intercalated ethanol and DMSO and, finally, the fourth peak centered at 516 °C (8.5%) due to the dehydroxylation of kaolinite (Tunney and Detellier, 1996; Brandt et al., 2003).

The first mass loss for sample Kaol–Pa occurred at 65 °C (3%), being attributed to the elimination of water and/or ethanol. The second process, between 150 and 287 °C (2%), was due to the removal of Pa

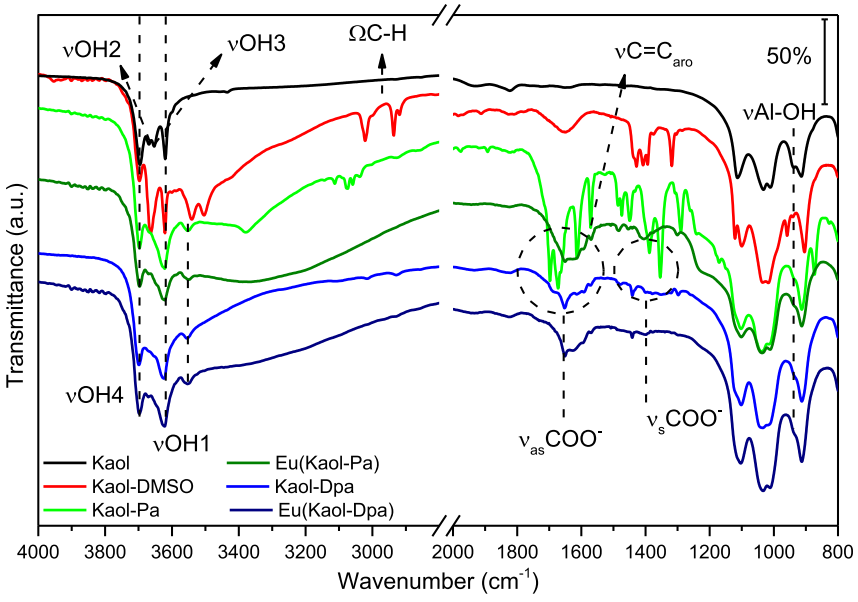

Fig. 2. Infrared absorption spectra (FTIR) of the different samples.

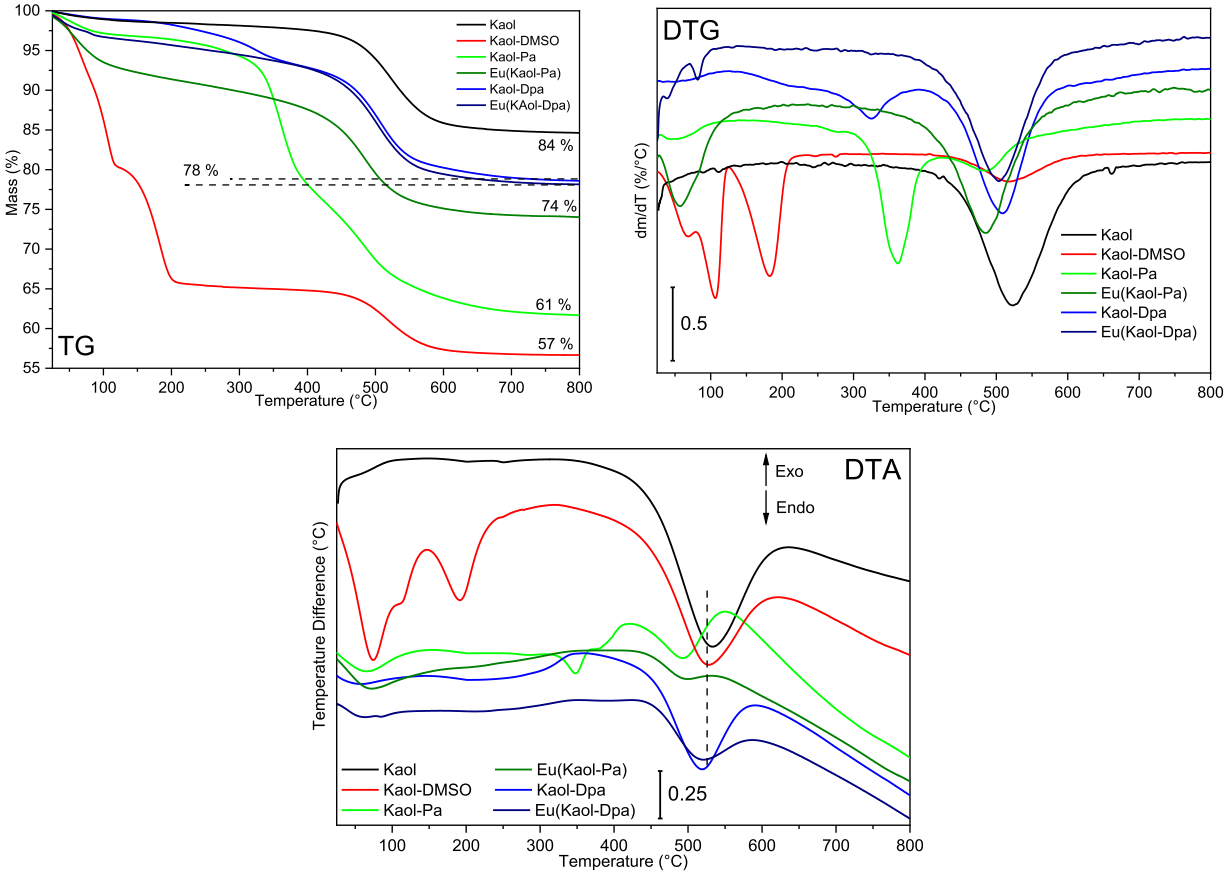

Fig. 3. Thermal curves of the different solids. DTG and DTA values were normalized between 0 and 1.

molecules that were adsorbed on the clay mineral surface. The third mass loss, centered at 362 °C (18%), was attributed to the decomposition of functionalized Pa molecules located in the interlayer space of the clay mineral. The fourth process, centered at 485 °C (14%), was due to kaolinite dehydroxylation. The approximate amount of Pa per minimum kaolinite formula was determined to be 0.54 mol. For the Kaol–Dpa sample, the elimination of intercalated Dpa took place between 135 and 240 °C (2%), the decomposition of the functionalized acid at 325 °C (4%) and kaolinite dehydroxylation at 509 °C (14.5%) (De Faria et al., 2012; Da Silva et al., 2016). The calculated amount of Dpa per kaolinite unit was 0.07 mol. The formulae for these compounds have been previously reported to be Ka–$(pa)_{1.59}$ and Ka–$(dpa)_{0.37}$, respectively (De Faria et al., 2009), i. e., the samples contain 1.59 and 0.74 carboxylic groups, respectively, per kaolinite unit cell, which could act for Eu^{3+} coordination. The main differences between the two samples may be associated to the washing strategy, as the Soxhlet procedure could induce a higher leaching of organic units. However, it is important to remark that covalently bonded units did not leach during the washing process, and the presence of Pa and Dpa moieties in the solids was confirmed by several techniques.

For the Eu–containing solids, the decomposition of pyridine–carboxylic acids started at about 330 °C; however, the DTA curve showed a peak centered around 485 °C for sample Eu(Kaol–Pa) and 503 °C for Eu(Kaol–Dpa). This effect corresponded to the simultaneous decomposition of organic matter and dehydroxylation of kaolinite. Complexation of the Eu(III) ion in the samples caused an evident increase in the thermal stability of the materials (Fig. 3).

Scanning electron microscopy (Fig. 4) showed the characteristic morphology of kaolinite clay mineral, with preferential formation of flat particles, hexagonal–shaped microcrystals parallel to the (001) planes, grouped into tactoids (De Faria et al., 2010), and an average particle diameter size (calculated by the ImageJ program) of 11 μm. In the functionalized solids, the particles were smaller, with an average diameter of 4 μm for sample Kaol–Pa and 3 μm for the Kaol–Dpa one; the primary particles seemed to be agglomerated resulting in a less ordered material, decreasing their crystallinity, as observed by XRD. The increase of the interlayer space by the intercalation of the pyridine–carboxylic acids, with the consequent weakening of the hydrogen bonds existing between the tetrahedral and octahedral layers, made more difficult the interaction between the layers (Li et al., 2015).

In the solids complexed with Eu^{3+} ions (Fig. 4 e and f) the particles were slightly smaller than in their precursor materials, showing average diameters of 2.5 μm for Eu(Kaol–Pa) and 2 μm for Eu(Kaol–Dpa), agglomerating in a higher extend and keeping the material more fragmented.

3.2. Luminescence spectroscopy

When the ligand absorbs energy to promote from the ground state (1S0) to an excited state, it can return to the ground state via radiative (fluorescence) or non–radiative (vibration and/or rotation) transitions, or the energy can be transferred to the triplet state ($^3T_1$). In this state, the ligand can transfer the energy to the Eu^{3+} ion by the antenna effect (Beltrán-Leiva et al., 2017; DeOliveira et al., 2007; Bala et al., 2018). This was clearly observed in excitation spectra of the synthesized solids (Fig. 5). When the emission was fixed at 617 nm (the characteristic wavelength of the $^5D_0 \rightarrow {}^7F_2$ transition, the most intense in the Eu (III) ion), Fig. 6, the characteristic transitions of Eu^{3+} ions due to transitions from the $^5D_0$ level to the ^7F_J (J = 0, 1, 2, 3, and 4) (Li and Yan, 2013; Binnemans, 2015) were recorded.

The spectra of Eu^{3+} ion complexes showed a single and broad band due to the $^5D_0 \rightarrow {}^7F_0$ transition, which was the result of the overlap of

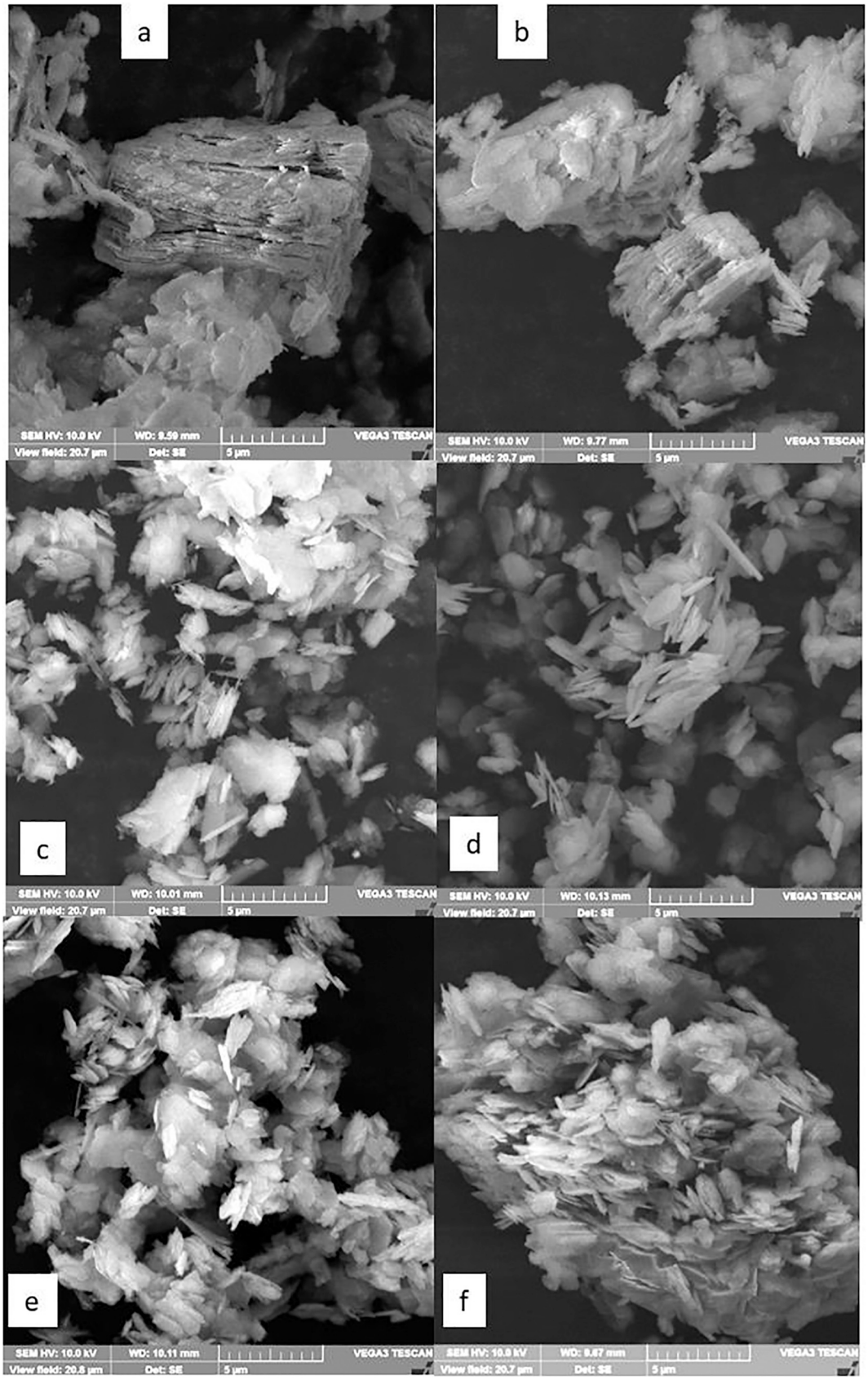

Fig. 4. SEM images with 10,000× magnification from Kaol (a), Kaol–DMSO (b), Kaol–Pa (c), Kaol–Dpa (d), Eu(Kaol–Pa) (e) and Eu(Kaol–Dpa) (f) solids.

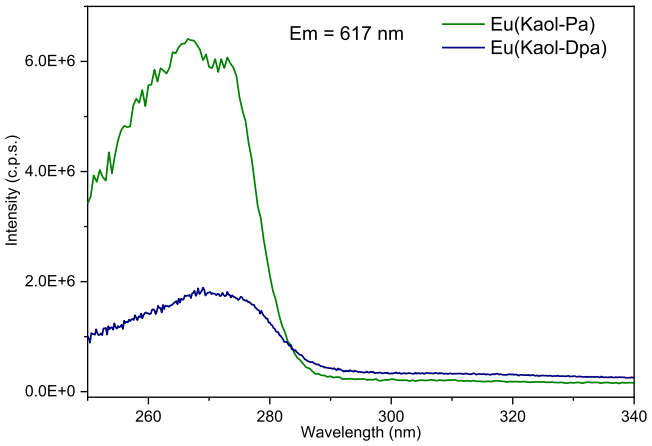

Fig. 5. Excitation spectra of luminescent hybrids Eu(Kaol–Pa) with slit = 2, and Eu(Kaol–Dpa) with slit = 3, at room temperature and 450 nm filter.

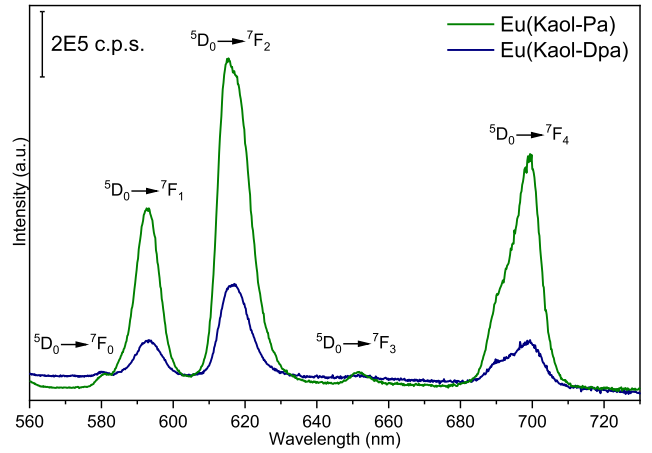

Fig. 6. Emission spectra of luminescent hybrids with the respective ascriptions. Eu(Kaol–Pa): $\lambda_{exc} = 266.5$ nm, $slit_{ex} = 3$, $slit_{em} = 3$; Eu(Kaol–Dpa):$\lambda_{exc} = 269.6$ nm, $slit_{ex} = 3$, $slit_{em} = 3$, at room temperature.

several bands indicating the presence of materials of polymeric nature or Eu^{3+} ions in several different sites (Buenzli and Choppin, 1989). Pyridine–carboxylic acids bonded to the kaolinite structure did not allow coordination to occur exactly as in isolated complexes, and thus, the existence of several possible coordination sites for the Eu(III) ion in the kaolinite immobilized ligands was confirmed. The transition $^5D_0 \rightarrow {}^7F_1$ was only slightly influenced by the coordination sphere, as it was allowed by the magnetic dipole mechanism and was independent of the environment of the ion, so it can be used as a standard to compare the other transitions (Zolin et al., 2004; Binnemans, 2009, 2015; Li and Yan, 2013). The relationship between the areas (A) of the bands due to the $^5D_0 \rightarrow {}^7F_0$ and $^5D_0 \rightarrow {}^7F_2$ transitions in relation to $^5D_0 \rightarrow {}^7F_1$, allowed to obtain information about changes that occurred around the ion, because the transitions $^5D_0 \rightarrow {}^7F_0$ and $^5D_0 \rightarrow {}^7F_2$ are of electrical dipole character and easily influenced by the chemical bonding of the ion and symmetry ((Binnemans, 2009).

It is also important to remark that Eu(dpa) and Eu(pa) are in a very confined space. The first coordination sphere of the complexes was not complete, as compared to pure isolated complexes $Na_3Eu(pa)_3$ and $Na_3Eu(dpa)_3$ (Figs. S1 and S2), due to the steric hindrance promoted by kaolinite confining interlayer spaces, as previous discussed (De Faria et al., 2012; De Araujo et al., 2017). Water molecules and OH groups from the kaolinite structure could remain coordinated in some positions of the coordination sphere in Eu(pa) and Eu(dpa) complexes. These coordinated species are essential for further exchange reactions in an aqueous medium, resulting in very good solids for sensing applications. This is in agreement with previous reports using clay minerals from the smectite group (Ma et al., 2019), that showed the displacement of some water molecules using immobilized complexes, resulting in an increase of emission intensity and lifetime, yielding highly luminescent materials.

From the values of the area ratios R_0 and R_2 (Table 2), changes in the symmetry within the first coordination sphere of the metal cation were deduced; the higher this value, the lower the symmetry of the complex and the greater the covalent character of the interaction between the ligand and the Eu^{3+} ion. According to Laporte's rule, electronic transitions via electric dipole are prohibited for states with the same parity, but by decreasing the symmetry of the ions this rule is relaxed; thus, from this ratio of peak areas, it can be concluded that the materials with smaller symmetries showed better emissions (De Araújo et al., 2020).

Regarding the Eu^{3+} ion emission lifetimes, a mathematical adjustment was made for the radiative decay curves. The second–order exponential regression used was suitable for both samples, showing the presence of more than one coordination sites, according to Eq. (1):

$$y = y0 + A1\left(^{-(x-x0)}/_{t1}\right) + A1\left(^{-(x-x0)}/_{t2}\right) \quad (1)$$

To calculate the internal quantum yield (η), the spontaneous emission coefficient ($A_{0\text{-}J}$) is required, that corresponds to the $^5D_0 \rightarrow {}^7F_J$ transition, according to Eq. (2) (Binnemans, 2015):

$$A_{0-J} = \frac{A_{0J} \cdot \nu_{01}}{I_{01} \cdot \nu_{0j}} .50\ s^{-1} \quad (2)$$

where $A_{0\text{-}J}$ is the spontaneous emission coefficient of the transition $^5D_0 \rightarrow {}^7F_J$; A_{0J} is the area of the emission band referring to the transition $^5D_0 \rightarrow {}^7F_J$; ν_{0J} is the barycenter (cm^{-1}) of the band on the transition $^5D_0 \rightarrow {}^7F_J$; I_{01} is the intensity of the average frequency of the emission band for the magnetic dipole transition $^5D_0 \rightarrow {}^7F_1$; and ν_{01} is the barycenter (cm^{-1}) relative to magnetic dipole transition $^5D_0 \rightarrow {}^7F_1$ (Binnemans, 2009). As already discussed, transition $^5D_0 \rightarrow {}^7F_1$ was taken as internal standards for the calculations, as it is a transition allowed by a magnetic dipole and is not influenced by the chemical environment. Thus, its coefficient of spontaneous emission was calculated as 50 s^{-1}. After calculating the spontaneous emission coefficient ($A_{0\text{-}J}$) it was possible to calculate the sum between radiative emissions (A_{rad}) and non–radiative transition probabilities (A_{nrad}) through Eq. (3) (Binnemans, 2015):

$$A_{total} = \frac{1}{\tau} = A_{rad} + A_{nrad} \quad (3)$$

where A_{total} is the total emission; A_{rad}, as already mentioned, refers to the radiative emissions and is calculated from the sum of the areas $\sum_j A_{0J}$, and finally the internal emission yield was calculated using Eq. (4) (Binnemans, 2015):

$$\eta = \frac{A_{rad}}{A_{total}} \quad (4)$$

The excited state lifetimes are directly influenced by the presence of water molecules coordinated to the central ion, promoting energy losses due to vibration processes with the O—H oscillators. This effect is much more pronounced in complexes containing ligands with less structural rigidity and in complexes with a high degree of hydration (Horrocks and Sudnick, 1979). Finally, an equation was elaborated to calculate the number of water molecules in the first coordination sphere of the Eu^{3+} ions considering the lifetime (τ_{rad}), acquired directly from the emission spectra and another from measurements in deuterated water. In this way, one can consider the experimental lifetime being τ_{H2O} and the radiative lifetime (without vibration losses) equal to τ_{D2O}, Eq. (5) (Binnemans, 2015; Supkowski and Horrocks, 2002, 1999):

Table 2
Radiative emission (A_{rad}), total emission (A_{total}), luminescence lifetime (τ), quantum yield (η), relation between areas (A) of the bands due to transitions $^5D_0 \rightarrow {}^7F_0$ (R_0) and $^5D_0 \rightarrow {}^7F_2$ (R_2) in relation to $^5D_0 \rightarrow {}^7F_1$ and quantity of water molecules (q) present in the synthesized luminescent hybrid materials.

Samples	A_{rad} (s^{-1})	A_{total} (s^{-1})	τ_1 (ms)	τ_2 (ms)	η_1 (%)	η_2 (%)	q	R_0	R_2
Eu(Kaol–Pa)	2058	6603	0.061	0.15	12.6	31.2	5	0.12	1.79
Eu(Kaol–Dpa)	2527	5593	0.003	0.18	0.7	45.2	3	0.44	1.98

$$q = 1.11\left[\frac{1}{\tau_{exp}} - \frac{1}{\tau_{rad}} - 0.31\right] \quad (5)$$

The spectroscopic data for the complexed hybrid materials are shown in Table 2. The number of water molecules coordinated to the Eu (III) ions calculated from luminescence spectroscopy were 5 and 3 for samples Eu(Kaol–Pa) and Eu(Kaol–Dpa), respectively. This result agreed with the thermal analyses data, in which the amount of water in sample Eu(Kaol–Pa) sample (8% by mass) was greater than in the Eu(Kaol–Dpa) sample (3% by mass), and also with the relative intensity of the water–related band at 3500 cm^{-1} in the FTIR spectra, more intense for sample Eu(Kaol–Pa).

3.3. Application as sensors for Cr^{3+}, ibuprofen and prometryn

Considering the luminescent properties of the synthesized materials, they were tested to evaluate their properties through the effect caused in the luminescence (increase or reduction of the emission intensity) upon adsorption of Cr^{3+} ion, ibuprofen and prometryn pollutants. The adsorption kinetics of the materials (Fig. 7) were determined by UV–Vis absorption spectroscopy.

The time to reach the equilibrium was shorter for the sample functionalized with picolinic acid, Eu(Kaol–Pa), than for that functionalized with dipicolinic acid (for Cr^{3+}, the behavior of both solids were identical). This difference can be attributed to the difference in the number of carboxylic groups in both compounds; as mentioned above, sample Eu (Kaol–Pa) had a larger number of carboxylic acid groups per mol of kaolinite. The luminescence of the materials was investigated at room temperature under excitation at 268 nm with emission in the red, and characteristic emissions of Eu^{3+} ions (Fig. 8), centered at 580, 593, 616, 651 and 699 nm, attributed to the transitions from $^5D_0$ to the states ^7F_J (J = 0, 1, 2, 3, and 4), respectively, were recorded, transition $^5D_0 \rightarrow {}^7F_2$ being the most intense.

The emission spectra (Fig. 8) showed that the luminescence of the samples was influenced by the adsorption of the pollutants, the luminescence intensity of the materials decreasing in the presence of the pollutants. Sample Eu(Kaol–Pa) was selective for ibuprofen, with an emission spectrum profile different from the others affecting the $^5D_0 \rightarrow {}^7F_2$ and $^5D_0 \rightarrow {}^7F_4$ transitions, as well as a variation in the ratio between the intensity of the $^5D_0 \rightarrow {}^7F_2$ transition in relation to that of the $^5D_0 \rightarrow$

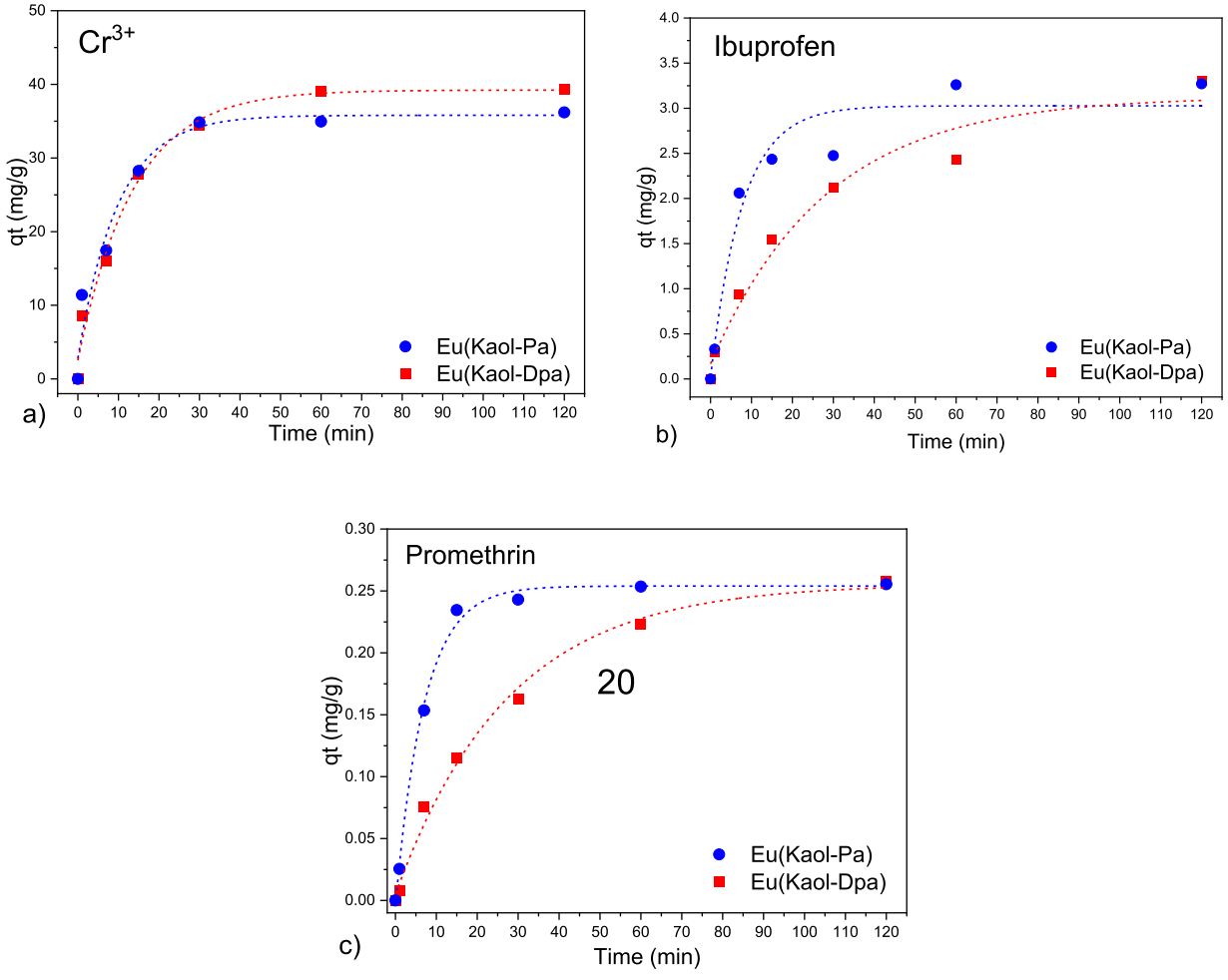

Fig. 7. Adsorption kinetics of the Cr^{3+} ion, ibuprofen and prometryn in the Eu(Kaol–Pa) and Eu(Kaol–Dpa) materials, respectively.

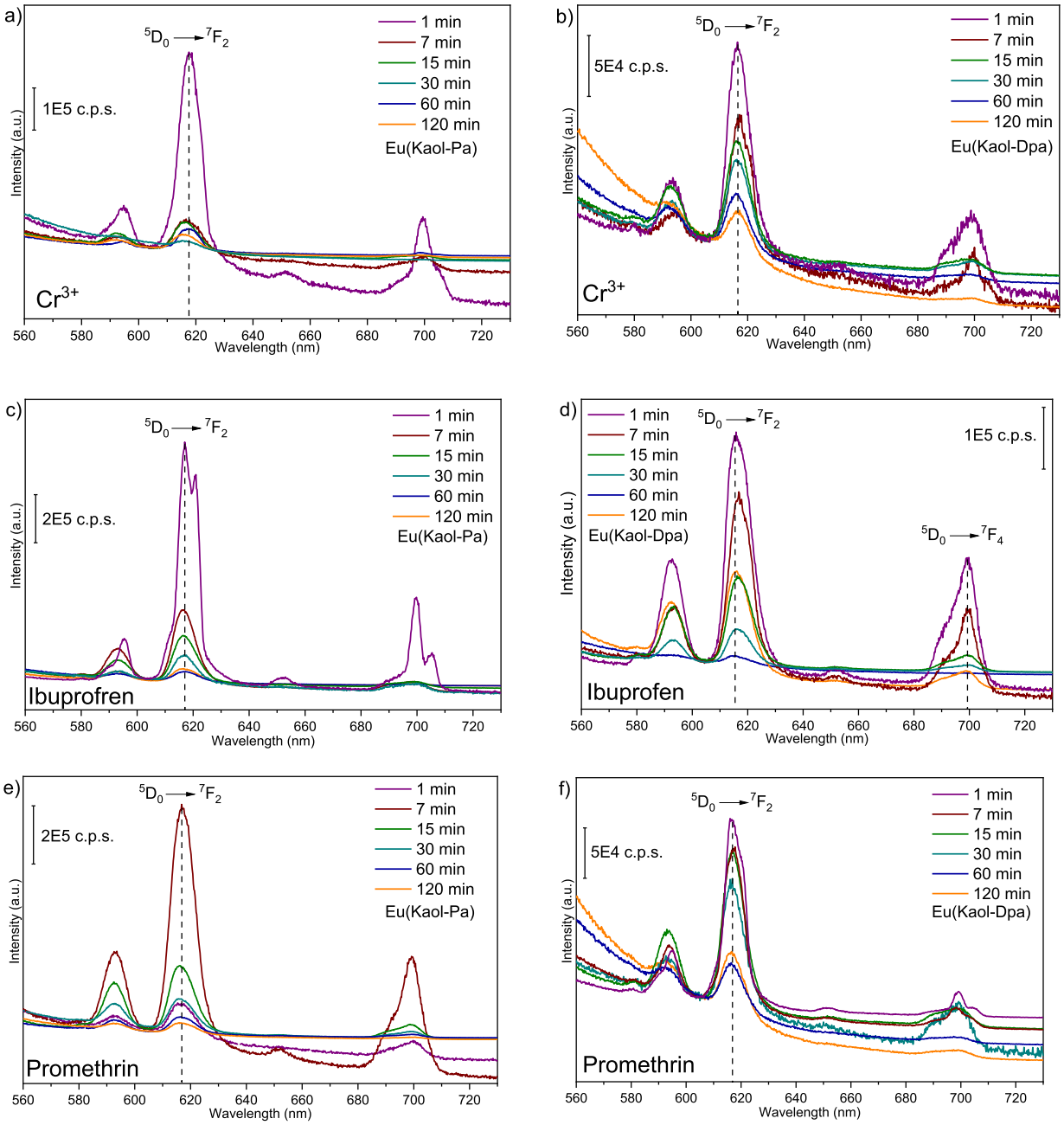

Fig. 8. Emission spectra of luminescent hybrids Eu(Kaol–Pa) (left) and Eu(Kaol–Dpa) (right) after adsorption of the indicated pollutants.

$^7F_1$ one, indicating that the drop in this relationship was directly linked to the concentration of the contaminant interacting with the luminescent complex (Fig. 9). The band between 470 and 500 nm observed in the emission spectra after contact with the contaminants, specially with Cr^{3+} for Eu(Kaol–pa) and Eu(Kaol–dpa), and with ibuprofen using Eu (Kaol–dpa) and for prometryn in both solids, was assigned to emission of contaminants adsorbed on Eu(Kaol–pa) and Eu(Kaol–dpa) solids and also to the emission of Kaol–pa and Kaol–dpa matrices; these broad bands are typical of organic ligands.

When incorporated into hybrid matrices, luminescent complexes may undergo luminescence suppression, due to the presence of –OH, –NH or –COOH groups or water molecules in the surface of these solids. This property was used to verify the range where the Eu^{3+} complexes showed a linear reduction of the emission intensity by non–radiative mechanisms, mainly by bonding to surface–OH groups and coordinated molecules to the potentially toxic metal Cr^{3+} (Zhan et al., 2019). In this way, the luminescence intensity curves of the most intense transition, $^5D_0 \rightarrow {}^7F_2$, were obtained as a function of the amounts adsorbed over time (Fig. S3), to assess whether there was any correlationship demonstrating that the materials behaved like a sensor in a certain sorption range.

By stipulating some ranges in the curves of Fig. 9 and Fig. S4, good linear relationships ($R^2 > 0.98$) were obtained between the intensity of the emission and the adsorbed quantity of each pollutant studied (Table 3). In these ranges, for a given absorption band, the amount of contaminant adsorbed by the materials was determined.

Regarding the adsorption of Cr^{3+} ions, the detection range of the materials was very different, between 0 and 17 mg g^{-1} for Eu(Kaol–Pa), but from 16 to 35 mg g^{-1} for Eu(Kaol–Dpa). The materials interacted with the $[Cr(H_2O)_6]^{3+}$ cation, removing water molecules from the first coordination sphere of the Eu(III) ions, causing a suppression of the luminescence through the vibrations of the water molecules. The range

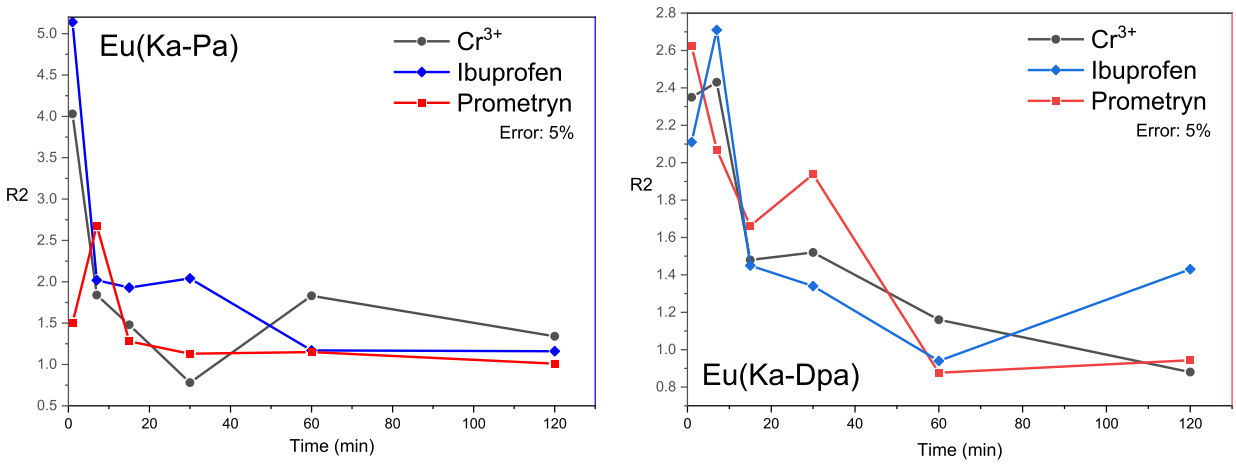

Fig. 9. Variation of the relation emission intensity R_2 ($^5D_0 \rightarrow {}^7F_2/{}^5D_0 \rightarrow {}^7F_1$) with time for samples Eu(Kaol–Pa) and Eu(Kaol–Dpa).

Table 3
Linear correlation data between the luminescence intensity of the synthesized hybrid materials and the adsorbed amounts of Cr^{3+}, ibuprofen and prometryn.

	Samples					
	Eu(Kaol–Pa)			Eu(Kaol–Dpa)		
Pollutants	Operation range (mg g^{-1})	R^2	a	Operation range (mg g^{-1})	R^2	a
Cr^{3+}	0–17	0.984	$-5.2{\cdot}10^5$	16–35	0.949	$-1.7{\cdot}10^3$
Ibuprofen	0.3–2.4	0.995	$-3.9{\cdot}10^5$	0.0–2.4	0.983	$-1.5{\cdot}10^5$
Prometryn	0.15–0.26	0.995	$-7.2{\cdot}10^5$	0.12–0.22	0.950	$-1.1{\cdot}10^6$

for ibuprofen was from 0 to 2.4 mg g^{-1} for the Eu(Kaol–Dpa), comprising 6 detection points, with a similar range for Eu(Kaol–Pa) (0.3 to 2.4 mg g^{-1}). As for prometryn, the correlation range for Eu(Kaol–Pa), comprising 5 measurement points, was between 0.15 and 0.26 mg g^{-1} and between 0.12 and 0.22 mg g^{-1} for Eu(Kaol–Dpa). Both prometryn and ibuprofen interacted with the complex through weak interactions such as Van der Waals interactions, increasing the oscillating groups present in the first coordination sphere, causing the suppression of luminescence. The different values of the angular coefficients (a) showed that each pollutant interfered in a different way with the materials (Fig. S5), ruling out that the relaxation of the luminescent intensity of each material was only due to the presence of water in the solutions of the tested adsorbates.

3.4. Photophysical Properties – Evaluation of the mechanism of detection by Eu(Kaol–pa) and Eu(Kaol–dpa) solids

To investigate the photophysical properties of the materials, the following parameters were determined: lifetime decay (τ) of the excited state $^5D_0$ of Eu^{3+} (Fig. S7) internal quantum efficiency (η_i), and number of water molecules (q) coordinated to the cations in the complexes (Table S1).

The presence of different oscillator groups in Eu–pa and Eu–dpa grafted on kaolinite could drastically influence the quantum efficiency results. These data agreed with the luminescence spectra and lifetime data, which, in turn, were compatible also with the number of water molecules coordinated to the Eu^{3+} ions; that is, the lifetime decreased when the oscillator groups promoted the quenching of Eu^{3+} ions promoting the nonradiative mechanism. Another interesting result is that the complexes Eu(Kaol–pa) and Eu(Kaol–dpa) presented mono–exponential fittings, which was assigned to very similar environments around the Eu^{3+} ions. However, in the presence of the contaminant, Cr^{3+}, ibuprofen and prometryn, the curves fitted very well with mono and bi–exponential adjusts. These data are in agreement with plots log (decay intensity) versus log (time) that showed different slopes, evidencing that more than one emission site were present in Eu (Kaol–pa) and Eu(Kaol–dpa) after contact with contaminants (Fig. S8). In other words, the presence of different quencher groups such as OH from hexa–aquo chromium (III) complexes and OH from ibuprofen or NH from prometryn promoted different effects around Eu^{3+} ions. As previously commented by Supkowski and Horrocks (2002) ligands containing N—H, O—H, or H–N–C=O oscillators can also shorten Eu^{3+} excited state lifetimes in different levels. This effect was clearly observed from the changes on lifetime values for each contaminant tested. The results were also in agreement with the emission spectra, as the intensities of the Eu^{3+} transitions changed drastically in the presence of each contaminant (see Fig. 8 from photoluminescence kinetic experiment with contaminants). The results of lifetime, quantum yield and number of water molecules present in each complex are summarized in Table S2.

These luminescence decay curves were well adjusted to bi–exponential functions, yielding the values of the pre–exponential terms (A1 and A2) that are assigned to the τ_1 and τ_2 components. This bi–exponential fit may be assigned to the heterogeneity of the chemical environment around Eu^{3+} ion in the complexes bonded to Kaol–pa and Kaol–dpa. After contact with contaminants for all of the solids studied here, the existence of two different emission sites, which were assigned to different complex species, can be concluded: one with a short lifetime (< 0.05 ms) and consequently a large number of coordinated water molecules and other oscillator groups (depending of each contaminant), and another with longer lifetime (>0.3 ms), that is, with a lower amount of coordinated water, and consequently having more pa or dpa ligands coordinated to the Eu^{3+} cations. Only prometryn with Eu(Kaol–pa) promoted the increase in the lifetime values and consequently increased the emission intensity of the solid due the effective coordination of the ligand to Eu^{3+} centers; as previously discussed (De Faria et al., 2009; De Araujo et al., 2017), the pa ligand bonded to kaolinite acted as a monodentate ligand, increasing the lability (the OH groups from the carboxylic acid were involved in covalent bonds with kaolinite), and only the nitrogen atom of the pyridine aromatic ring is able to coordinate the Eu^{3+} cation. This point reinforced that prometryn could act via chelate effect and promote the stabilization of the Eu^{3+} ion, as a complex

prometryn may be induced by chelation–enhanced luminescence quenching. The prometryn molecule contains five nitrogen atoms in its structure, each having a lone pair of electrons to donate (acting as a Lewis base). Additionally, it is important to remark that the ring containing nitrogen (between two substituents at the 4th and 6th positions of the ring) is known to be more basic in comparison to the nitrogen atom of the amino group and it can coordinate easily with different metal ions, inducing the removal of water molecules from complexes and increasing the lifetime values and the internal quantum efficiency. It is important to highlight also that due to the presence of large bands in the emission spectra recorded after contact with contaminants, it cannot be discarded that other competitive mechanisms could be responsible for these effects, such as formation of new complexes, and quenching induced by other organic groups from clay and contaminants. The quenching of the hypersensitive peak of Eu^{3+} ($^5D_0 - {}^7F_2$) at 616 nm with certain contaminants (Cr^{3+}, ibuprofen and prometryn) confirmed the selectivity of the luminescent sensor. On the other hand, for the Eu–(Kaol–dpa) series, the quenching effects are remarkable for all the contaminants tested; the dpa ligand presented two carboxylic groups and one of them was chemically bonded to the clay surfaces and the other remained able to interact with the Eu^{3+} ion.

In spite of these data, obtained from the equations available for calculation, we do not believe that these values really translate what is happening in practice with sensors Eu(Kaol–pa) and Eu(Kaol–dpa), since it is believed (Horrocks and Sudnick, 1979; Supkowski and Horrocks, 2002) that not all quencher groups will present the same effect as water (even water bound to Cr^{3+} will be different). The NH group from prometryn or OH group from ibuprofen will present a different effect, so this evaluation could not be general, since the complex itself has changed (after complexation with contaminants) and therefore the chemical environment of Eu^{3+} changed too. This no longer allows these equations to be used.

It is important to remark also that UV–Visible spectra of all supernatant liquids (Fig. S9) resulted from adsorption experiments after vigorous magnetic stirring with contaminants, did not shown the typical bands of Eu–pa or Eu–dpa complexes. This fact corroborated the hypothesis that no leaching of active sites from sensors occurred during adsorption; the reduction on lifetime values, and the reduction on emission intensities resulted from coordination with active sites and exchange of water molecules by new ligands on Eu(Kaol–pa) and Eu (Kaol–dpa) solids. It should be also highlighted that the precursors were exhaustively washed (including via Soxhlet using ethanol and water) and only the pa and dpa units covalently bonded remained in the kaolinite.

The ratio between the areas of the bands due to the $^5D_0 \rightarrow {}^7F_0$ and $^5D_0 \rightarrow {}^7F_2$ transitions relative to the intensity of the band due to the $^5D_0 \rightarrow {}^7F_1$ transition provided important information about the changes in the environment around the Eu^{3+} ion (Table S2). The $^5D_0 \rightarrow {}^7F_0$ and $^5D_0 \rightarrow {}^7F_2$ transitions have an electric–dipole character, and the intensities of the bands due to these transitions heavily depend on the bonds established by the ion (Joos et al., 2015; Binnemans, 2015; De Araujo et al., 2017). However, the $^5D_0 \rightarrow {}^7F_1$ transition is allowed by a magnetic–dipole mechanism, and its intensity is scarcely influenced by the coordination environment of the cation and could be used as a sort of standard to measure the relative intensities of the other bands in the emission spectrum (Joos et al., 2015, Binnemans, 2015, De Araujo et al., 2017). The ratio between the intensities of the bands $^5D_0 \rightarrow {}^7F_0$ / $^5D_0 \rightarrow {}^7F_1$ and $^5D_0 \rightarrow {}^7F_2$ / $^5D_0 \rightarrow {}^7F_1$ allowed to estimate the symmetry of the complex: The higher values of ratios resulting in the lower the symmetry and vice versa. It is important to remark that in Eu^{3+} complexes higher values of the $^5D_0 \rightarrow {}^7F_2/{}^5D_0 \rightarrow {}^7F_1$ evidence the lower symmetry of the complex and the higher the covalent character of the Eu^{3+}–ligand interaction. Table S2 lists the results concerning these ratios and the difference between each contaminant tested.

Comparing the precursors used here, the higher values of ratios were obtained for the Eu(Kaol–pa) solid, nearby 19.35, compared to Eu (Kaol–dpa), 7.18. This difference clearly evidenced the different environment of coordination of Eu^{3+} around mono and dicarboxylic ligand.

For the Eu(Kaol–pa) sample, after contact with Cr^{3+}, ibuprofen and prometryn, respectively, the intensity ratio $^5D_0 \rightarrow {}^7F_2/{}^5D_0 \rightarrow {}^7F_1$ decreased from 19.35 to 1.04, 0.72 and 1.59, respectively. For Eu (Kaol–dpa), this ratio decreased from 7.18 to 2.41, 1.28 and 1.66, respectively. It is important to remark that the contaminants could induce the breakage of some pa or dpa bonds from the Eu^{3+}–complexes, resulting in differences around the Eu^{3+} ions. This effect was clearly observed in Eu(Kaol–pa) solids, that showed the higher relative decreasings, probably due to the presence of one unique coordination site to Eu^{3+} on Kaol–pa (nitrogen from the pyridine ring). On the other hand, the Eu(Kaol–dpa) presented lower decreasings, evidencing that Eu–dpa had more stable chemical bonds with kaolinite surfaces.

3.5. Characterization of the solids after adsorption experiments: Sensing mechanism

Fig. 10A and B show the FTIR spectra of Kaol–pa, and Kaol–dpa precursors complexed with Eu^{3+} ions, Kaol–pa(Eu) and Kaol–dpa(Eu) samples, and of the solids resulting after sensing experiments with Cr^{3+}, prometryn and ibuprofen. The infrared spectra of pure kaolinite (not shown) displayed four bands in the 3700–3500 cm^{-1} region (3694, 3668, 3650, 3618 cm^{-1}), assigned to the stretching mode of the inter– and intralamellar hydroxyl groups (Frost, 1996; Tunney and Detellier, 1996; Letaief et al., 2008; Dedzo and Detellier, 2016). The shift of these bands evidenced the intercalation of molecules in this region. In Kaol–pa and Kaol–dpa hybrid materials, the typical bands of the antisymmetric and symmetric stretching modes of the carboxylate groups were also observed at 1689, 1566, and 1478 cm^{-1} (De Faria et al., 2009). The presence of more than two typical bands of the carboxylate groups (symmetric and antisymmetric) could be assigned to different interactions of these carboxylate groups in the interlayer space of kaolinite (a highly dipolar environment), which could induce the interaction via hydrogen bonds and changing the vibrational modes of carboxylate groups nonbonded to kaolinite surfaces. Another significant change occurred in this region between 1600 and 1300 cm^{-1}, induced by the presence of contaminants (prometryn, chromium and ibuprofen) that interacted effectively with the polar end of pa and dpa molecules and resulted in changes in the vibration bands of carboxylate.

The main differences after the sensing experiments were the shift of the typical bands of carboxylate groups between 1700 and 1300 cm^{-1}, evidencing that changes occurred in the coordination environment of Eu–pa and Eu–dpa complexes. This fact could be assigned to various reasons: i) The water molecules could be changed by new oscillator groups from the contaminants, such as OH from carboxylic acids (ibuprofen) and from aqueous Cr^{3+}–complexes or NH groups from prometryn; ii) The magnetic stirring could result in an increased exposure of the carboxylic acid groups grafted on the kaolinite surface, inducing to contaminant species and water molecules; iii) In the specific case of Cr^{3+}, the possibility of cation exchange of Cr^{3+} by Eu^{3+} cannot be ruled out, and also the possible coordination of free carboxylic groups of Cr^{3+} that could act as a quencher, inducing the reduction of luminescence. The possible complexation with Cr^{3+} was evidenced by the bands attributed to the stretching modes of the C—N, C—O and C—H bonds, that shifted from 1649, 1615, 1570, 1480–1454, 1345, and 1297 cm^{-1} to 1678, 1642, 1604, 1499–1480, and 1290 cm^{-1}, thereby confirming the coordination of Cr^{3+} to the N atom and the carboxylate group of the picolinate and dipicolinate groups grafted on kaolinite. The band observed close to 1705 cm^{-1} was ascribed to the C═O stretching vibration of pa and dpa free carboxylic acid groups, evidencing that no–bonded species are available on clay mineral surfaces and can induce the pre–concentration of contaminants via dipolar interactions promoting the sensing effect. It is important to remark that the typical interlamellar OH kaolinite bands (938 cm^{-1}) were not observed in the spectra of both solids, which confirmed that the carboxylic acids

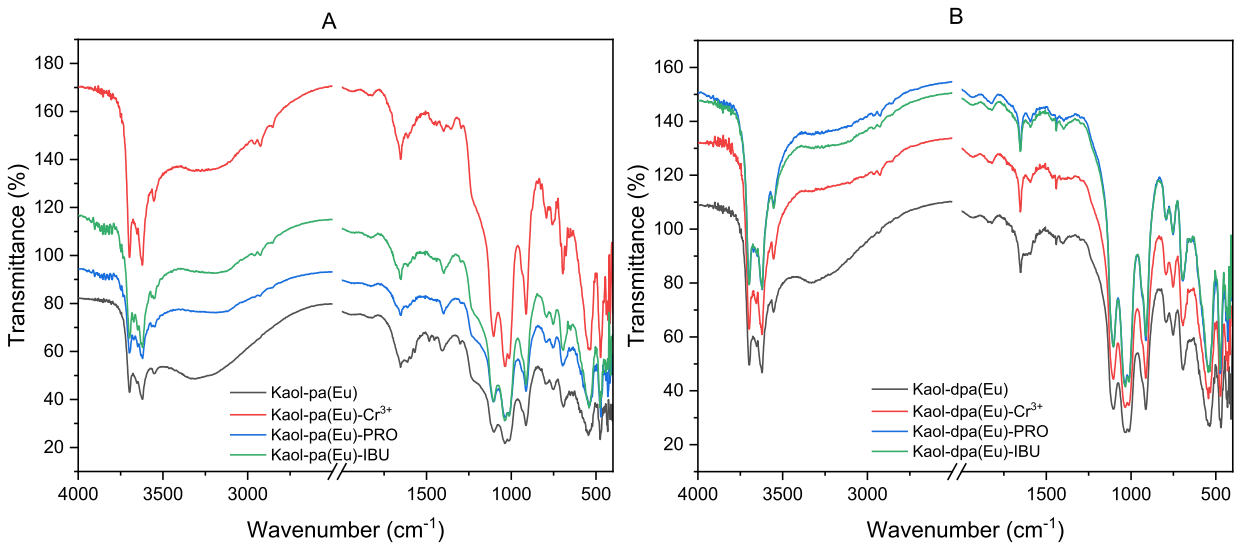

Fig. 10. Quantitative FTIR analysis of Kaol–pa(Eu) and Kaol–dpa(Eu) series before and after adsorption experiments with Cr^{3+}, prometryn and ibuprofen.

remained bonded to the kaolinite surfaces, as also evidenced by the OH stretching bands in the 3500 to 3700 cm^{-1} range. This agreed with previous data concerning the characterization of kaolinite–luminescent materials, and confirmed the higher stability resulting from covalent bonds established between carboxylic acids and Al–OH groups from kaolinite, forming Al–O–C bonds (De Faria et al., 2011, 2009, 2012; De Araujo et al., 2017). Fig. S6 summarizes the proposed mechanism involved in the luminescence quenching effect based on this characterization of the post–adsorption solids.

4. Conclusions

The kaolinite–functionalized ligands led to the achievement of promising inorganic–organic hybrids, with greater thermal stability than the isolated materials. Kinetic and equilibrium studies were carried out for Eu^{3+} adsorption by complexation, which allowed to investigate the complexation mechanisms, determining the optimal adsorption time for each material. The best reaction parameters were obtained after 24 h and a concentration of $8{\cdot}10^{-1}$ mol L^{-1} of $EuCl_3$ solution (maximum tested condition) for Kaol–Pa that had a higher adsorption capacity, and 48 h with a concentration of $5{\cdot}10^{-1}$ mol L^{-1} for Kaol–Dpa. The materials had been synthesized by a simple, low–cost route, and exhibited long lifetime and internal quantum yield of radiative emission.

The contact of the materials with Cr^{3+}, ibuprofen or prometryn caused a suppression of the luminescence intensity. Correlations were obtained, for certain absorption bands, when analyzing the adsorption kinetics of these pollutants simultaneously with luminescence; so, these materials may act as quantitative sensors for these pollutants, allowing to determine the amount of contaminant adsorbed by the materials. The best behavior was shown by the Eu(Kaol–Pa) sample for ibuprofen, being highly selective, showing a emission spectrum as a function of time totally different from those of the other pollutants.

Author statement

All the authors have participated in all the parts of this work. This work belongs to the Ph. D. Thesis of DTA, carried out in the "Cotutela PhD" modality at both Univerdade de Franca and Universidad de Salamanca, supervised by EHF and MAV. By this reason, DTA was the author most intensely involved in the experimental section of the paper and in the elaboration of the results, always under the supervision of EHF and MAV. The work was developed in the laboratories of both Universities, all the other authors belongs to these laboratories and has actively participated in the development of the experiments, in the elaboration of the results, and in the preparation and discussion of the different versions of the manuscript.

Declaration of Competing Interest

The authors declare that they have no known competing financial interests or personal relationships that could have appeared to influence the work reported in this paper.

Acknowledgements

The Brazilian group acknowledges the support from research funding agencies Fundação de Amparo à Pesquisa do Estado de São Paulo, FAPESP (2013/19523–3 and 2017/15482–1), and Coordenação de Aperfeiçoamento de Pessoal de Nível Superior (CAPES) finance code 001 and Conselho Nacional de Desenvolvimento Científico e Tecnológico, CNPq (311767/2015–0 and 303135/2018–2). The equipments of Brazilian group have been financed by FAPESP (1998/11022–3, 2005/00720–7, 2011/03335–8, 2012/11673–3 and 2016/01501–1). DTA thanks Universidade de Franca and Universidad de Salamanca for a "Cotutela PhD" facilities and FAPESP grants (2017/01719–0, 2018/26569–3).

Appendix A. Supplementary data

Supplementary data to this article can be found online at https://doi.org/10.1016/j.clay.2022.106591.

References

Avila, L.R., de Faria, E.H., Ciuffi, K.J., Nassar, E.J., Calefi, P.S., Vicente, M.A., Trujillano, R., 2010. New synthesis strategies for effective functionalization of kaolinite and saponite with silylating agents. J. Colloid Interface Sci. 341, 186–193.
Aydar, S., Bayraktepe, D.E., Filik, H., Yazan, Z., 2018. A Nano-Sepiolite Clay Electrochemical Sensor for the Rapid Electro-Catalytic Detection of Hydroquinone in Cosmetic Products. Acta Chim. Slov. 65, 946–954.
Bala, M., Kumar, S., Devi, R., Taxak, V.B., Boora, P., Khatkar, S.P., 2018. Synthesis and photoluminescence properties of europium(III) complexes sensitized with β–diketonato and N, N-donors ancillary ligands. Spectrochim. Acta Part A Mol. Biomol. Spectrosc. 196, 67–75.
Bates, K.E., Lu, H., 2016. Optics-Integrated Microfluidic Platforms for Biomolecular analyses. Biophys. J. 110, 1684–1697.
Beltrán-Leiva, M.J., Cantero-López, P., Zúñiga, C., Bulhões-Figueira, A., Páez-Hernández, D., Arratia-Pérez, R., 2017. Theoretical method for an accurate elucidation of energy transfer pathways in europium(III) complexes with

dipyridophenazine (dppz) ligand: one more step in the study of the molecular antenna effect. Inorg. Chem. 56, 9200–9208.
Binnemans, K., 2009. Lanthanide-based luminescent hybrid materials. Chem. Rev. 109, 4283–4374.
Binnemans, K., 2015. Interpretation of europium(III) spectra. Coord. Chem. Rev. 295, 1–45.
Brandt, K.B., Elbokl, T.A., Detellier, C., 2003. Intercalation and interlamellar grafting of polyols in layered aluminosilicates. D-Sorbitol and adonitol derivatives of kaolinite. J. Mater. Chem. 13, 2566.
Buenzli, J.C.G., Choppin, G.R., 1989. Lanthanide Probes in Life, Chemical a Earth Sciences: Theory and Practice. Elsevier.
Chen, X., Wang, Y., Chai, R., Xu, Y., Li, H., Liu, B., 2017. Luminescent lanthanide-based organic/inorganic hybrid materials for discrimination of glutathione in solution and within hydrogels. ACS Appl. Mater. Interfaces 9, 13554–13563.
Da Silva, A.C., Ciuffi, K.J., dos Reis, M.J., Calefi, P.S., de Faria, E.H., 2016. Influence of physical/chemical treatments to delamination of nanohybrid kaolinite-dipicolinate. Appl. Clay Sci. 126, 251–258.
Danish, S., Kiran, S., Fahad, S., Ahmad, N., Ali, M.A., Tahir, F.A., Rasheed, M.K., Shahzad, K., Li, X., Wang, D., Mubeen, M., Abbas, S., Munir, T.M., Hashmi, M.Z., Adnan, M., Saeed, B., Saud, S., Khan, M.N., Ullah, A., Nasim, W., 2019. Alleviation of chromium toxicity in maize by Fe fortification and chromium tolerant ACC deaminase producing plant growth promoting rhizobacteria. Ecotoxicol. Environ. Saf. 185, 109706.
De Araujo, D.T., Ciuffi, K.J., Nassar, E.J., Vicente, M.A., Trujillano, R., Calefi, P.S., Rives, V., de Faria, E.H., 2017. Eu^{3+}- and Tb^{3+}-dipicolinate complexes covalently grafted into kaolinite as luminescence-functionalized clay hybrid materials. J. Phys. Chem. C 121, 5081–5088.
De Araújo, D.T., de Pádua, G.S., Peixoto, V.G., Ciuffi, K.J., Nassar, E.J., Vicente, M.A., Trujillano, R., Rives, V., Pérez-Bernal, M.E., de Faria, E.H., 2020. Luminescent properties of biohybrid (kaolinite-proline) materials synthesized by a new boric acid catalyzed route and complexed to Eu^{3+}. Appl. Clay Sci. 192, 105634.
De Faria, E.H., Lima, O.J., Ciuffi, K.J., Nassar, E.J., Vicente, M.A., Trujillano, R., Calefi, P. S., 2009. Hybrid materials prepared by interlayer functionalization of kaolinite with pyridine-carboxylic acids. J. Colloid Interface Sci. 335, 210–215.
De Faria, E.H., Ciuffi, K.J., Nassar, E.J., Vicente, M.A., Trujillano, R., Calefi, P.S., 2010. Novel reactive amino-compound: Tris(hydroxymethyl)aminomethane covalently grafted on kaolinite. Appl. Clay Sci. 48, 516–521.
De Faria, E.H., Nassar, E.J., Ciuffi, K.J., Vicente, M.A., Trujillano, R., Rives, V., Calefi, P. S., 2011. New highly luminescent hybrid materials: terbium pyridine−picolinate covalently grafted on kaolinite. ACS Appl. Mater. Interfaces 3, 1311–1318.
De Faria, E.H., Ricci, G.P., Marçal, L., Nassar, E.J., Vicente, M.A., Trujillano, R., Gil, A., Korili, S.A., Ciuffi, K.J., Calefi, P.S., 2012. Green and selective oxidation reactions catalyzed by kaolinite covalently grafted with Fe(III) pyridine-carboxylate complexes. Catal. Today 187, 135–149.
Dedzo, G.K., Detellier, C., 2016. Functional nanohybrid materials derived from kaolinite. Appl. Clay Sci. 130, 33–39.
DeOliveira, E., Neri, C.R., Serra, O.A., Prado, A.G.S., 2007. Antenna effect in highly luminescent Eu^{3+} anchored in hexagonal mesoporous silica. Chem. Mater. 19, 5437–5442.
Di Baccio, D., Pietrini, F., Bertolotto, P., Pérez, S., Barcelò, D., Zacchini, M., Donati, E., 2017. Response of *Lemna gibba* L. to high and environmentally relevant concentrations of ibuprofen: removal, metabolism and morpho-physiological traits for biomonitoring of emerging contaminants. Sci. Total Environ. 584–585, 363–373.
Dorledo de Faria, R.A., Douaud, A., Soares, R.B., Dias Heneine, L.G., Matencio, T., de Freitas Cunha Lins, V., Messaddeq, Y., 2020. Electrochemical behavior of screen-printed carbon electrodes as transducers in biosensors. Corrosion 76, 553–561.
Ferreira, B.F., Ciuffi, K.J., Nassar, E.J., Vicente, M.A., Trujillano, R., Rives, V., de Faria, E. H., 2017. Kaolinite-polymer compounds by grafting of 2-hydroxyethyl methacrylate and 3-(trimethoxysilyl)propyl methacrylate. Appl. Clay Sci. 146, 526–534.
Frost, R.L., 1996. The dehydroxylation of the kaolinite clay minerals using infrared emission spectroscopy. Clay Clay Miner. 44, 635–651.
Gonzalez-Rey, M., Tapie, N., Le Menach, K., Dévier, M.-H., Budzinski, H., Bebianno, M.J., 2015. Occurrence of pharmaceutical compounds and pesticides in aquatic systems. Mar. Pollut. Bull. 96, 384–400.
Horrocks, W.D., Sudnick, D.R., 1979. Lanthanide ion probes of structure in biology. Laser-induced luminescence decay constants provide a direct measure of the number of metal-coordinated water molecules. J. Am. Chem. Soc. 101, 334–340.
Jasrotia, D., Singh, B., Kumar, A., Verma, S.K., Alvi, P.A., Kumar, K., Sridhar, B., 2019. $[HgCl_4]^{2-}$ $[C_5H_6N_2Cl]^{2+}$ inorganic-organic hybrid material with structural and optical properties. Results Phys. 14, 102421.
Jia, P., Wang, Z., Zhang, Y., Zhang, D., Gao, W., Su, Y., Li, Y., Yang, C., 2020. Selective sensing of Fe3+ ions in aqueous solution by a biodegradable platform based lanthanide metal organic framework. Spectrochim. Acta Part A Mol. Biomol. Spectrosc. 230, 118084.
Joos, J.J., Poelman, D., Smet, P.F., 2015. Energy level modeling of lanthanide materials: review and uncertainty analysis. Phys. Chem. Chem. Phys. 17, 19058–19078.
Lapides, I., Yariv, S., 2009. Thermo-X-ray-diffraction analysis of dimethylsulfoxide-kaolinite intercalation complexes. J. Therm. Anal. Calorim. 97, 19–25.
Letaief, S., Detellier, C., 2007. Nanohybrid materials from the intercalation of imidazolium ionic liquids in kaolinite. J. Mater. Chem. 17, 1476.
Letaief, S., Tonle, I.K., Diaco, T., Detellier, C., 2008. Nanohybrid materials from interlayer functionalization of kaolinite. Application to the electrochemical preconcentration of cyanide. Appl. Clay Sci. 42, 95–101.
Lezhnina, M., Benavente, E., Bentlage, M., Echevarría, Y., Klumpp, E., Kynast, U., 2007. Luminescent hybrid material based on a clay mineral. Chem. Mater. 19, 1098–1102.
Li, Q.-P., Yan, B., 2013. Novel luminescent hybrids by incorporating rare earth β-diketonates into polymers through ion pairing with an imidazolium counter ion. Photochem. Photobiol. Sci. 12, 1628.
Li, X., Liu, Q., Cheng, H., Zhang, S., Frost, R.L., 2015. Mechanism of kaolinite sheets curling via the intercalation and delamination process. J. Colloid Interface Sci. 444, 74–80.
Li, P., Li, Z., Li, H., 2016. Emission fingerprint relationships of low-level water in organic solvents based on Ln^{3+}-β-diketonate complexes in laponite. Adv. Optical Mater. 4, 156–161.
Liu, J., Ji, G., Xiao, J., Liu, Z., 2017. Ultrastable 1D europium complex for simultaneous and quantitative sensing of Cr(III) and Cr(VI) ions in aqueous solution with high selectivity and sensitivity. Inorg. Chem. 56, 4197–4205.
Ma, J., Yang, D., Song, X., Wang, Y., 2019. Luminescent materials of covalent grafting lanthanide complexes to the synthetic clays. J. Lumin. 212, 126–132.
Marchesi, S., Bisio, C., Carniato, F., 2021. Enhancement of the luminescence properties of Eu (III) containing paramagnetic saponite clays. Appl. Sci. 11, 8903.
Mbey, J.A., Thomas, F., Ngally Sabouang, C.J., Liboum, Njopwouo, D., 2013. An insight on the weakening of the interlayer bonds in a Cameroonian kaolinite through DMSO intercalation. Appl. Clay Sci. 83–84, 327–335.
Mbokana, J.G.Y., Dedzo, G.K., Ngameni, E., 2020. Grafting of organophilic silane in the interlayer space of acid-treated smectite: Application to the direct electrochemical detection of glyphosate. Appl. Clay Sci. 188, 105513.
Peña-Guzmán, C., Ulloa-Sánchez, S., Mora, K., Helena-Bustos, R., Lopez-Barrera, E., Alvarez, J., Rodriguez-Pinzón, M., 2019. Emerging pollutants in the urban water cycle in Latin America: a review of the current literature. J. Environ. Manag. 237, 408–423.
Rives, V., 2001. Layered Double Hydroxides: Present and Future, 1st ed. Nova Science Publishers.
Sas, S., Danko, M., Lang, K., Bujdák, J., 2015. Photoactive hybrid material based on kaolinite intercalated with a reactive fluorescent silane. Appl. Clay Sci. 108, 208–214.
Sato, H., Tamura, K., Yamagishi, A., 2014. Luminescent oxygen gas sensors based on nanometer-thick hybrid films of iridium complexes and clay minerals. Chemosensors 2, 41–55.
Shanker, A., Cervantes, C., Lozatavera, H., Avudainayagam, S., 2005. Chromium toxicity in plants. Environ. Int. 31, 739–753.
Sharma, S., Bhattacharya, A., 2017. Drinking water contamination and treatment techniques. Appl Water Sci 7, 1043–1067.
Su, Y., Zhang, D., Jia, P., Gao, W., Li, Y., He, J., Wang, C., Zheng, X., Yang, Q., Yang, C., 2019. Bonded-luminescent foam based on europium complexes as a reversible copper (II) ions sensor in pure water. Eur. Polym. J. 112, 461–465.
Supkowski, R.M., Horrocks, W.D., 1999. Displacement of Inner-Sphere Water molecules from Eu^{3+} analogues of Gd^{3+} MRI contrast agents by carbonate and phosphate anions: dissociation constants from luminescence data in the rapid-exchange limit. Inorg. Chem. 38, 5616–5619.
Supkowski, R.M., Horrocks, W.D., 2002. On the determination of the number of water molecules, q, coordinated to europium(III) ions in solution from luminescence decay lifetimes. Inorg. Chim. Acta 340, 44–48.
Takahashi, K., 1964. Spectrophotometric determination of rare earth elements with Xylenol Orange. Bunseki Kagaku 13, 343–346.
Tang, W., Zhang, Y., Bai, J., Li, J., Wang, J., Li, L., Zhou, T., Chen, S., Rahim, M., Zhou, B., 2020. Efficient denitrification and removal of natural organic matter, emerging pollutants simultaneously for RO concentrate based on photoelectrocatalytic radical reaction. Sep. Purif. Technol. 234, 116032.
Tonlé, I.K., Diaco, T., Ngameni, E., Detellier, C., 2007. Nanohybrid kaolinite-based materials obtained from the interlayer grafting of 3-aminopropyltriethoxysilane and their potential use as electrochemical sensors. Chem. Mater. 19, 6629–6636.
Tronto, J., Ribeiro, S.J.L., Valim, J.B., Gonçalves, R.R., 2009. Visible and near-infrared luminescent Eu^{3+} or Er^{3+} doped laponite-derived xerogels and thick films: Structural and spectroscopic properties. Mater. Chem. Phys. 113, 71–77.
Tunney, J.J., Detellier, C., 1996. Chemically modified kaolinite. Grafting of methoxy groups on the interlamellar aluminol surface of kaolinite. J. Mater. Chem. 6, 1679.
Utochnikova, V.V., 2019. The use of luminescent spectroscopy to obtain information about the composition and the structure of lanthanide coordination compounds. Coord. Chem. Rev. 398, 113006.
Wang, K.M., Du, L., Ma, Y.L., Zhao, J.S., Wang, Q., Yan, T., Zhao, Q.H., 2016. Multifunctional chemical sensors and luminescent thermometers based on lanthanide metal-organic framework materials. CrystEngComm 18, 2690–2700.
Wang, Y., Li, P., Wuang, S., Li, H., 2019. Recent progress in luminescent materials based on lanthanide complexes intercalated synthetic clays. J. Rare Earths 37, 451–467.
Whittaker, M.L., Lammers, L.N., Carrero, S., Gilbert, B., Banfield, J.F., 2019. Ion exchange selectivity in clay is controlled by nanoscale chemical–mechanical coupling. Proc. Natl. Acad. Sci. 116, 22052–22057.
Xiang, S., Bao, D.-X., Wang, J., Li, Y.-C., Zhao, X.-Q., 2017. Luminescent lanthanide coordination compounds with pyridine-2,6-dicarboxylic acid. J. Lumin. 186, 273–282.
Yang, D., Liu, J., Wang, Q., Hong, H., Zhao, W., Chen, S., Yan, C., Lu, H., 2019. Geochemical and probabilistic human health risk of chromium in mangrove sediments: a case study in Fujian, China. Chemosphere 233, 503–511.

Zhan, Z., Liang, X., Zhang, X., Jia, Y., Hu, M., 2019. A water-stable europium-MOF as a multifunctional luminescent sensor for some trivalent metal ions (Fe^{3+}, Cr^{3+},Al^{3+}), PO_4^{3-} ions, and nitroaromatic explosives. Dalton Trans. 48, 1786–1794.
Zhang, S., Liu, Q., Cheng, H., Li, X., Zeng, F., Frost, R.L., 2014. Intercalation of dodecylamine into kaolinite and its layering structure investigated by molecular dynamics simulation. J. Colloid Interface Sci. 430, 345–350.
Zolin, V.F., Puntus, L.N., Tsaryuk, V.I., Kudryashova, V.A., Legendziewicz, J., Gawryszewska, P., Szostak, R., 2004. Spectroscopy of europium and terbium pyridine-carboxylates. J. Alloys Compd. 380, 279–284.